

POLITECNICO DI TORINO

Corso di Laurea Magistrale in Ingegneria Biomedica



**Politecnico
di Torino**

Tesi di Laurea Magistrale

Coupling of multibody models and finite element models to investigate the role of muscles in the in silico prediction of femoral fracture risk

Supervisors

Dr. Alessandra ALDIERI

Dr. Mara TERZINI

Prof. Cristina BIGNARDI

Candidate

Francesco Mattia BRUNO

March 2024

Abstract

Femoral fractures pose a significant challenge to public health, especially in light of the increasing number of elderly subjects affected by osteoporosis worldwide. In this context, when aiming to predict femoral fracture *in silico*, it is still not clear whether muscles actions have a protective effect on the fracture risk or, on the contrary, those increase the fracture risk. Hence, aiming to evaluate the contribution of muscles forces in this context, this thesis focused on exploring various approaches described in the literature to transfer muscles forces from a multibody model to a finite element (FE) model of the femur. In particular, several methods to constrain the FE model were analysed. An Opensim-derived simplified musculoskeletal model was used to simulate a static pose and calculate the muscle forces directly acting on the femur. These forces were then applied to a femur's FE model simulating a fall on the side, by constraining the femur in five different ways based on literature studies. The FE model comprised a force applied on the centre of the femoral head with a frictionless contact defined between the greater trochanter and a rigid plane. Distally, the following five constraint cases were considered: 1) the reference case boundary conditions, where the diaphysis nodes were linked to the knee centre, modelled as a hinge, through beams elements; 2) all the nodes in the distal portion of the femur were fully constrained; 3) three nodes in the mid-diaphysis were fully constrained; 4) one node near the patella groove was constrained in antero-posterior displacements, the most distal node of the medial condyle was fully constrained, and the most distal node at the lateral condyle was constrained in antero-posterior and cranio-caudal displacements; 5) the node on the femoral head's surface, referred to as the hip contact node, was constrained in antero-posterior and cranio-caudal displacements; additionally, one node near the patella groove was fully constrained, and a node on the distal lateral epicondyle was constrained in antero-posterior displacement. All these models were also compared to the reference model, where case 1) boundary conditions were applied but without any muscles forces applied. Principal strains represented the references biomechanical variables considered to perform the comparisons. The five cases considered with applied muscle forces showed 0.247% ($\pm 0.343\%$), 0.248% ($\pm 0.341\%$), 0.232% ($\pm 0.313\%$), 0.285% ($\pm 0.390\%$), 0.085% ($\pm 0.207\%$) average values for the maximum principal strain, and -0.253% ($\pm 0.346\%$), -0.254% ($\pm 0.343\%$), -0.238% ($\pm 0.313\%$), -0.290% ($\pm 0.392\%$), -0.087% ($\pm 0.130\%$) average values for the minimum principal strains. The FE model without muscles forces instead showed 0.248% ($\pm 0.333\%$) and -0.253% ($\pm 0.335\%$) average values for the maximum and minimum principal strains, respectively.

Table of Contents

List of Tables	III
List of Figures	IV
Acronyms	VII
1 Introduction	1
1.1 Multibody model	2
1.2 Finite Element model	4
1.3 MB and FE model integration	5
2 Material and methods	12
2.1 Implementation of Multibody model	12
2.1.1 Muscle and Joint Reaction forces calculation	14
2.1.2 Resultant Forces and Moments calculation	15
2.2 FE model: Boundary and Load conditions	16
2.2.1 Simulation cases	18
3 Results and discussion	22
3.1 Analysis of Principal Strains	22
3.2 Visual and Statistical Analysis	24
4 Conclusion	36
Bibliography	37

List of Tables

2.1	The twelve selected muscles with their relative maximum isometric force (MIF) that the fiber can generate.	14
2.2	Simulation cases.	17
3.1	Strain Mean and Standard Deviation of maximum strains (ϵ_1). . . .	23
3.2	Strain Mean and Standard Deviation of minimum strains (ϵ_3). . . .	23
3.3	p-values obtained from the Kolmogorov-Smirnov test comparing the maximum strains (ϵ_1) and the fitted distribution of the study cases with the reference case. p-values in the first column were derived directly from the distribution data, while p-values in the second column were derived from fitted distribution data.	34
3.4	p-values obtained from the Kolmogorov-Smirnov test comparing Case 0 with cases 1, 2, 3, and 4 for the maximum strains (ϵ_1) and the fitted distribution. p-values in the first column were derived directly from the distribution data, while p-values in the second column were derived from fitted distribution data.	34
3.5	p-values obtained from the Kolmogorov-Smirnov test comparing the minimum strains (ϵ_3) and the fitted distribution of the study cases with the reference case. p-values in the first column were derived directly from the distribution data, while p-values in the second column were derived from fitted distribution data.	34
3.6	p-values obtained from the Kolmogorov-Smirnov test comparing Case 0 with cases 1, 2, 3, and 4 for the minimum strains (ϵ_3) and the fitted distribution. p-values in the first column were derived directly from the distribution data, while p-values in the second column were derived from fitted distribution data.	35

List of Figures

1.1	OpenSim’s basic multibody model of the musculoskeletal system in the lower limbs [6].	2
1.2	In a walking OpenSim[9] model, markers (shown in pink) serve as virtual reference points, allowing for the identification and tracking of specific positions on the human body, which allows for motion capture.	3
1.3	Example: stresses in a plate with a hole solved using various element sizes.	4
1.4	Color map visualization of the FE model’s strains [5].	5
1.5	Applying the muscle and joint forces to the finite element model [5].	6
1.6	Muscle and joint forces of musculoskeletal model (left) transferred to finite element model (right) [15].	7
1.7	The entire finite element model with muscles as single straight lines. Shaded elements represent the four element levels used in the detailed strain analysis [13].	8
1.8	Contributions of individual muscles to strain in the middle portion of the femoral neck, calculated for different tasks for a representative subject [16].	9
1.9	Top: muscle sets included in the analysis. Bottom: oblique view of the femur solid model showing the location of node constraints for each configuration. [17].	10
2.1	Representation of muscles that were directly in contact with the femur. Global coordinate system: X(Red), Y(Green), Z(Blue). (A.) On the left, the complete model with all muscles. On the right the same model but with the selected twelve muscles. (B.) On the right, the complete model with all muscles. On the left the same model but with the selected twelve muscles.	13
2.2	Local coordinate system. X(Red), Y(Green), Z(Blue)	14
2.3	Output from OpenSim utilized in the MATLAB script.	15

2.4	Load condition for the <i>reference case</i> : load force applied to the centre of femoral head (green arrow).	16
2.5	Load condition for all the cases except for the reference case. Muscle forces applied to the FE model surface (red arrows). For all the muscle forces, the three component (x,y,z) were considered. Load force applied to the centre of femoral head (green arrow).	17
2.6	Boundary conditions for case 0: hinge at the knee node (in orange) linked to a selection of diaphysis nodes through beams elements (in black). Black arrows represent biomechanical length [22][23][24]. . .	18
2.7	Boundary conditions for Case 1: all the nodes (selection in yellow) in the distal portion of the femur were fully constrained (in pink) [5][15].	18
2.8	Boundary conditions for Case 2: three selected nodes from the femur's mid-diaphysis are shown in the top image (in red); the three selected nodes were fully constrained (in pink), shown in the bottom image [17].	19
2.9	Boundary conditions for Case 3. Three selected nodes: in purple the most distal node at the lateral condyle, in red the most distal node of the medial condyle and in blue the patella groove node in the top image. The most lateral node (purple) was constrained in X and Y displacements, the most medial node (red) was fully constrained and the patella groove node (blue) was constrained in X displacements, shown in the bottom image [5].	20
2.10	Boundary conditions for Case 4: Three nodes selected: node on the femoral head's surface, referred to as the hip contact node (red), a node on the distal lateral epicondyle (purple) and one node near the patella groove (blue).	21
2.11	On the left: the node on the distal lateral epicondyle was constrained in X displacement and the node near the patella groove was fully constrained. On the right: The node on the femoral head's surface, referred to as the hip contact node, was constrained in X and Y displacements [17].	21
3.1	Region of interest for the analysis of the results. The lateral part of the greater trochanter is excluded due to boundary conditions effect, with the biomechanical length indicated by the black arrow.	22
3.2	Maximum strains distribution within the region of interest. Strains are shown for all the cases. It is shown the isometric view of the femur.	25

3.3	Minimum strains distribution within the region of interest. Strains are shown for all the cases. It is shown the isometric view of the femur.	26
3.4	Comparison of strain distributions in various cases. The reference case is shown in purple, with the other five cases in the following order: blue, green, yellow, red, and aquamarine. The figure shows the boxplots of the maximum strains (ϵ_1).	27
3.5	Comparison of strain distributions in various cases. The reference case is shown in purple, with the other five cases in the following order: blue, green, yellow, red, and aquamarine. The figure shows the boxplots of the minimum strains (ϵ_3).	28
3.6	Comparison of strain distributions in various cases. The reference case is shown in purple, with the other five cases in the following order: blue, green, yellow, red, and aquamarine. The figure shows the histograms of the maximum strains (ϵ_1).	29
3.7	Comparison of strain distributions in various scenarios. The reference case is shown in purple, and the other five cases are in the following order: blue, green, yellow, red, and aquamarine. The figure depicts the histograms of the minimum strains (ϵ_3). The absolute value of the data was taken.	30
3.8	Histograms of deformation data overlaid with fitted gamma distribution curves. The y-axis represents the probability density function (PDF), while the x-axis shows $\mu\epsilon$ values. The fitted curves closely match the observed data distribution for maximum strains (ϵ_1) across all analyzed cases.	32
3.9	Histograms of deformation data overlaid with fitted gamma distribution curves. The y-axis represents the probability density function (PDF), while the x-axis shows $\mu\epsilon$ values. The fitted curves closely match the observed data distribution for minimum strains (ϵ_3) across all analyzed cases.	33

Acronyms

BC

Boundary Conditions

CT

Computed Tomography

DOF

Degrees Of Freedom

FE

Finite Element

JCF

Joint Contact Force

MB

Multibody

MIF

Max Isometric Force

MRI

Magnetic Resonance Imaging

PDF

Probability Density Function

SD

Standard Deviation

Chapter 1

Introduction

The relationship between muscle strength and the risk of bone fracture is emerging as a fundamental field of study, especially considering the increasingly high incidence of fractures. Furthermore, femoral fractures are a significant public health challenge, especially in elderly populations with osteoporosis. Skeletal integrity is essential for these people in order to keep their bones healthy and avoid fractures. Muscles not only provide structural support and stability to bones, but their contractility and ability to absorb impacts can play a crucial role in fracture prevention and in maintaining skeletal integrity. This aspect is influenced by the musculature, in particular low muscle strength is considered a major predictor of fragility fractures and that the musculature plays a crucial role in maintaining skeletal integrity [1]. Muscle strength play a protective role in reducing the risk of falls and related injuries, including fractures of the femoral neck, in particular Harvey et al.[2] findings highlight the importance of considering muscle density as an independent risk factor for fractures. Osteoporosis is closely related to sarcopenia, with bone weakening associated with muscle aging in terms of fiber atrophy and physical activity reduction. Sarcopenia is considered one of the major responsible factors for functional limitations and motor dependency in elderly osteoporotic individuals. Physical activity should be strongly recommended in osteoporotic patients at diagnosis.

This thesis represents a preliminary investigation aimed at understanding the role of the muscles in femoral fracture prediction. Specifically, the focus has been on testing various methods outlined in the literature to transition from a *multibody* (MB) model to a *finite element* (FE) model. In conclusion, a comparison of the different methods is carried out with an emphasis on the principal strains produced by muscle forces on the surface of the femur.

1.1 Multibody model

A multibody model is a computational representation of a system consisting of multiple interconnected bodies, such as bones, joints, and muscles, to simulate their motion and interactions. Multibody models describe the behavior of the system using kinematic relations and equations derived from Newton's second law, which determine the motion based on applied forces and changes in momentum [3].

These models are particularly useful for simulating musculoskeletal systems, as they can capture large translational and rotational displacements, making them ideal for studying movements and forces in the human body. Infact they are mathematical models that describes the motion and interaction of multiple bodies, taking into account their mass, geometry, and constraints [4]. Multibody models are frequently used to study changes in motion and their effects on important internal structures, such as the femur. These models also incorporate personalized gait data and muscle forces [5]. Anatomical reference locations and positions are obtained from imaging techniques such as computed tomography (CT) and magnetic resonance imaging (MRI).

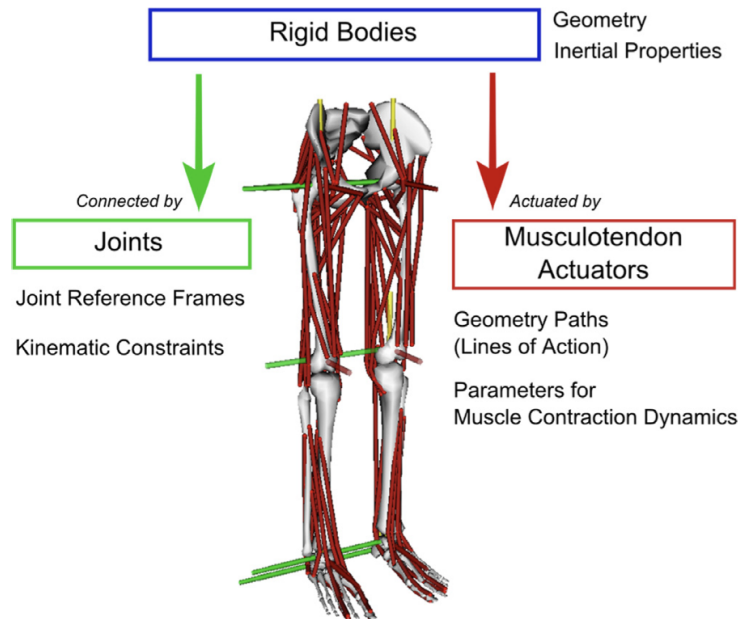


Figure 1.1: OpenSim's basic multibody model of the musculoskeletal system in the lower limbs [6].

The analysis of kinematics, kinetics, and the effects of outside forces is made possible by these models, which incorporate the concepts of rigid body dynamics and can simulate the motion and forces experienced by each body in the system

(figure 1.1 taken by Valente et al. study [6]). In fact multibody modeling, that can be applied to model the musculoskeletal system, enabling estimations of muscle and joint reaction forces that are difficult to measure experimentally. Motion capture-based musculoskeletal models can be created using measured marker trajectories (Figure 1.2) and ground reaction forces, allowing for analysis of gait modifications on the specific joint compressive forces [7]. Thus, these models can be used to better understand how particular movements or situations affect the musculoskeletal system, which can help, for instance, with the creation of injury prevention plans and rehabilitation plans. However, these models are occasionally oversimplified in order to accelerate simulations, which prevents any clinically meaningful conclusions to be derived. In simply, a multibody model by itself might not be adequate to faithfully capture the physiological activities of a particular mechanism [8]. Software tools for musculoskeletal modeling have aided in the growth of such applications. OpenSim [9], an open-source software platform, has been increasingly used as a reference tool for musculoskeletal simulations of movement. It also allows for the sharing and distribution of models. As personalized medicine has become more popular, there has been an increase in subject-specific musculoskeletal modeling with varying levels of customization [10][11].

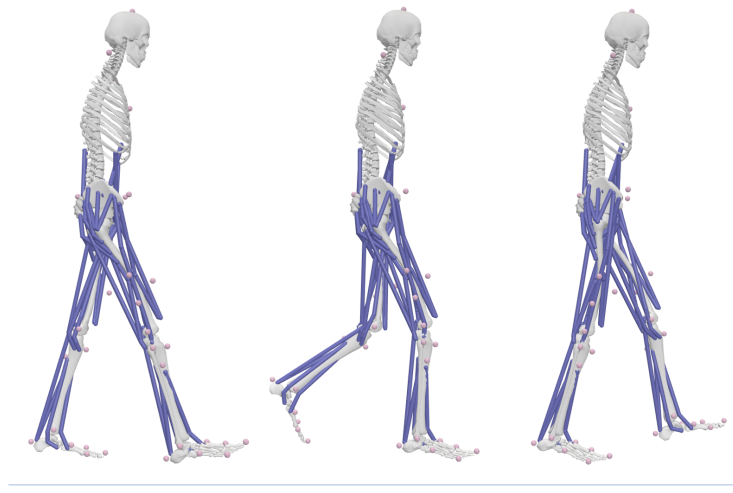


Figure 1.2: In a walking OpenSim[9] model, markers (shown in pink) serve as virtual reference points, allowing for the identification and tracking of specific positions on the human body, which allows for motion capture.

1.2 Finite Element model

A finite element model is a computational representation of a physical system or structure and its basic concept is the discretisation (division) of complex mechanical structures into finite numbers of separate components with simple geometry called *elements* [8], to simulate its behavior under various conditions [4]. Individual elements in the FE method are connected together by a topological map known as a *mesh*, and the fields within the element are represented using a local polynomial. The solution obtained is a function of mesh quality (Figure 1.3), with the fundamental requirement that the mesh conform to the geometry [12]. The FE method was first developed to solve elasticity and structural analysis problems in 1940s.

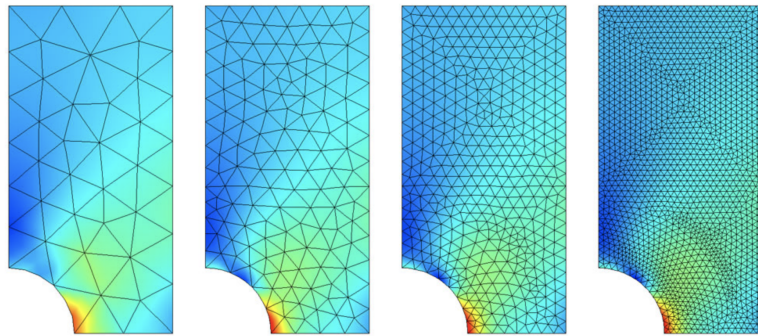


Figure 1.3: Example: stresses in a plate with a hole solved using various element sizes.

In this way, complex nonlinear problems become solvable numerically. Nowadays, the FE method has been widely used in different engineering fields for system design and analysis. Over the past decades, the FE method has also been increasingly used for investigating a large range of problems in biomechanics and orthopaedics to analyze stress, strain, deformation, and other physical phenomena in structures, fluids, and materials. The techniques of finite element analysis are utilized to determine how the system will react to applied loads or boundary conditions (BC). In fact, the FE methods's main advantage is that it can easily handle complex BCs.

For instance, the finite element model was used by Altai et al.[5] for the prediction of principal strains, which represent the deformation and stress distribution within the femoral neck during different phases of the gait cycle [5] (Figure 1.4). Accurate estimation of strain distribution using the finite element model is important for understanding the loading patterns and potential risks to the femoral neck during daily activities. In another study [13], the FE model was used to evaluate the different distributions on the surface of the femur, specifically comparing the load with all thigh muscles included to the simplified load regimes at 30% of the gait

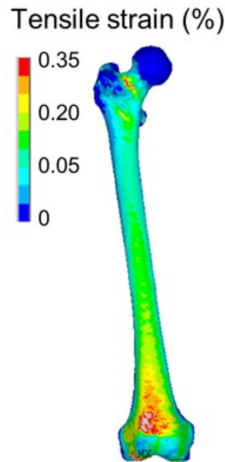


Figure 1.4: Color map visualization of the FE model's strains [5].

cycle for four levels along the femoral shaft. Thus, using a FE model provides a significant advantage in understanding the biomechanical behavior of the human femur under different loading conditions, allowing for a detailed assessment of strains, deformations, and muscle interactions.

1.3 MB and FE model integration

A combined musculoskeletal-finite element modeling approach can provide a more accurate picture of the mechanical response of the femur during daily activities, which can help optimize clinical decision making. Accurate estimation of physiological strain distribution can also help predict patient-specific parameters, such as bone strength and joint load, using non-invasive medical imaging and gait data [5]. This information can be valuable in improving treatment outcomes and developing personalized interventions for individuals with bone and joint conditions.

A pipeline for a fully customized multiscale model was created by Altai et al.[5] to study the strain levels at the femoral neck during a typical walking cycle. They collected CT and MRI scans of the lower limb, as well as gait data, were collected for all participants. Body level musculoskeletal models were used to derive muscle forces. Finite element femur models were constructed to analyze the strain levels at the femoral neck. BC on the finite element femur models were implemented using muscle forces obtained from the musculoskeletal models. Because the FE model's deflections alter the moment arm of applied forces and prevent the force set from being entirely equilibrated, BCs are required to bring the model into equilibrium [14]. Making sure the model is statically definite is one crucial rule. In other words, the FE model cannot be allowed to freely spin or move. Errors accumulated

in both the musculoskeletal model and the finite element model, as well as the assumption to conduct quasi-static analysis through the gait cycle [5]. Altai et al. refer to these computational errors as *residual forces*. In this study [5], forces were applied at the surface mesh node that was closest to the point of application that the musculoskeletal model estimated; the location of the attachment point of each muscle was specifically estimated by the musculoskeletal model. The distance varied between 0.1 and 1.6 mm between the closest nodes in the finite element model and the point of application of the forces. The finite element models were kinematically constrained at the distal end of the femur to prevent rigid body motion. These constraints were chosen to get the residual values as small as possible or close to zero. Two different boundary conditions for the finite element model were tested:

- a. The distal end of the femur was totally fixed;
- b. Three selected nodes were constrained (Figure 1.5) as follow:
 - The most distal node of the medial condyle was completely fixed;
 - The displacement of the most distal node at the lateral condyle was constrained in the anterior-posterior and craniocaudal directions;
 - The node in the patella groove was constrained antero-posteriorly.



Figure 1.5: Applying the muscle and joint forces to the finite element model [5].

These boundary conditions (b) were chosen with the goal of simulating the fundamental gait patterns of walking: abduction-adduction primarily at the hip joint, flexion-extension, and rotation at the knee and ankle joints.

The current study aimed to investigate the mechanical response of the femur during a normal walking cycle using a fully personalized coupled body-organ modeling method. Multibody dynamics models were used to calculate muscular and joint contact forces, while the finite element method was used to predict deformations in the femoral neck during flat terrain walking. This study included five participants to investigate the interindividual variability of predicted deformation patterns.

In another study, S. Martelli examined femoral neck strain during maximal isometric contraction of the hip-spanning muscles using verified musculoskeletal and finite element models [15]. The study tried to investigate femoral neck strain during maximal isometric contraction of the hip-spanning muscles. The musculoskeletal and femur finite-element models from an elderly white woman were derived from previous studies. Hip-spanning muscles were divided into six groups based on their function. The femoral neck strain was calculated by fully activating the agonist muscles at fourteen physiological joint angles. Using an internal procedure, S. Martelli applied muscle and joint reaction forces to the finite element model; this transfer is shown in Figure 1.6 below.

The finite element model of the femur was distally fully constrained. The force vector was expressed in the femoral coordinate system.

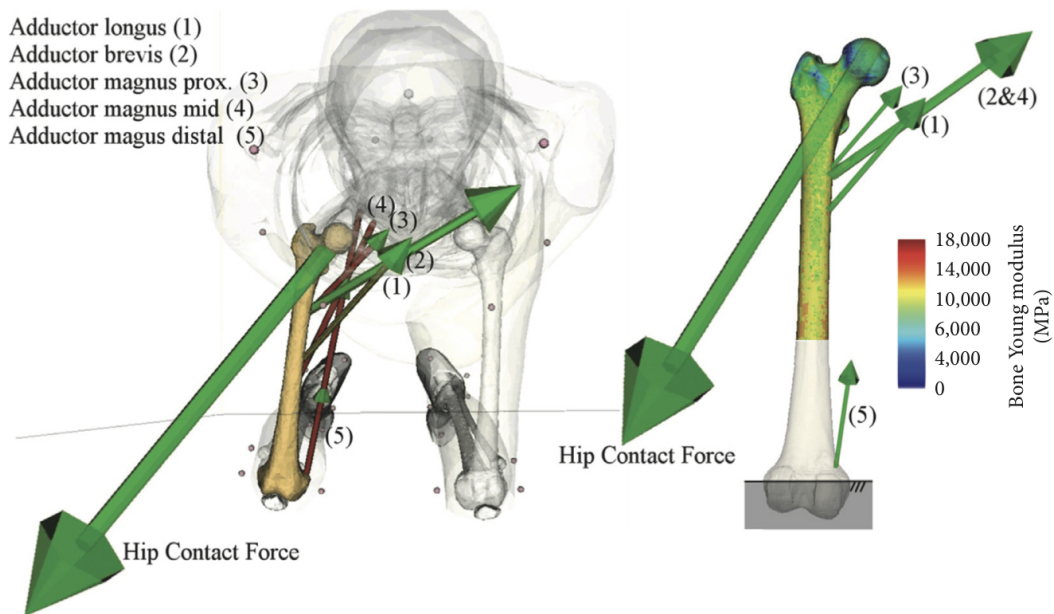


Figure 1.6: Muscle and joint forces of musculoskeletal model (left) transferred to finite element model (right) [15].

The purpose of this study of S. Martelli was to investigate the hypothesis that

the muscles crossing the hip could cause a specific distribution of muscle and postural tensions in the proximal femur. To accomplish this, stress models of the femoral neck were calculated during maximal isometric contractions of the hip-crossing muscles across a physiological range of motion for an average elderly Caucasian woman. The main maps of tensile and compressive stress were compared in terms of magnitude and regional distribution, which are known to influence the extent and spatial location of bone mechanical adaptation.

A crucial aspect of studying the interface between multibody and FE models is achieving force equilibrium also after applying the forces in the FE model. This point is highlighted in the Duda et al. study case [13]. In particular, in this study, the equilibrium of loads was disturbed by scaling the muscle attachment data to the Standardized Femur. The tibio-femoral contact force was increased by roughly 3% of its initial value in order to reestablish force equilibrium. The tibio-femoral contact force was distributed to nodes on the lateral and medial condyles. The equilibrium of moments was achieved by distributing the magnitude of these contact forces unequally between both condyles and by slightly increasing the gluteus maximus (force 1.14 times its original value).

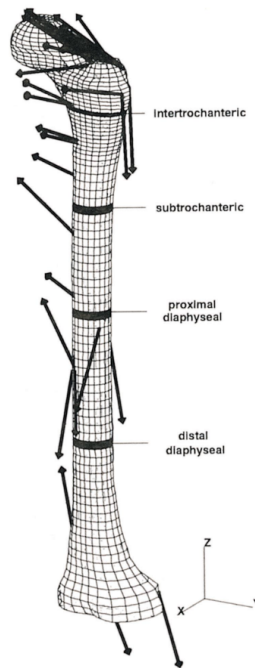


Figure 1.7: The entire finite element model with muscles as single straight lines. Shaded elements represent the four element levels used in the detailed strain analysis [13].

Since the model was completely balanced, also for this study, only rigid body

motions were restricted by fixing three nodes on the distal end of the bone. In regard to muscle attachment data, force magnitudes and orientations, they were derived from the literature [13] and scaled to the Standardized Femur model [13]. Only those muscles attaching to the femur were included as single straight lines and made to match appropriate node coordinates (Figure 1.7). In particular, a single force vector that was applied to the ventral groove between the femoral condyles was formed by combining the forces of the vasti, rectus femoris, and patellar ligament.

The study's goal was to determine strain distribution during walking while taking into account the load on all thigh muscle groups. It aimed to compare these distributions to those obtained with simplified loads and determine which muscles should be included in simulations to accurately represent loading conditions on the proximal femur with the greatest physiological relevance.

As seen in the previous studies, combining multibody models and FE models can be very useful, another proof of that is given by the study conducted by M.E.Kersh et al. [16]. They used them to investigate the femoral neck loading condition in order to find the answer for this question '*which muscles are important for loading areas of bone that are prone to fracture?*'. In particular, they wanted to identify the specific muscles loading the femoral neck during five different activities.

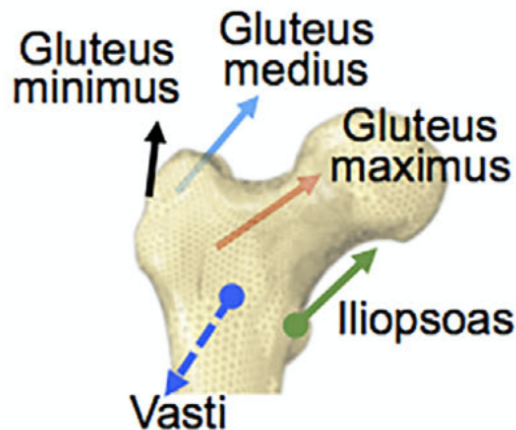


Figure 1.8: Contributions of individual muscles to strain in the middle portion of the femoral neck, calculated for different tasks for a representative subject [16].

Experimental data were recorder thanks to bipolar surface electrodes, for the activity of 11 muscles, and by reflective markers, for collecting kinematic data. All the analysis to the multibody scaled model were performed using OpenSim [9]. The muscle forces and hip joint reaction force from each subject's musculoskeletal model were applied as boundary conditions to the individualized finite element

models. The hip joint force was applied as a point vector at the femoral head surface defined by the hip contact force vector passing through the hip joint center. The muscle force components were then applied at the node closest to the muscle attachment point in the finite element model (Figure 1.8). Also for this study the distal end of the femur was fully constrained to prevent any displacement.

The choice of boundary conditions influence both the strain magnitudes and the mode of deflection of the intact femur, this is the conclusion reached by Speirs et al. in their study [17]. In this study the purpose was to show the influence of various commonly used boundary conditions and to propose a physiologically based constraint configuration that minimises reaction forces at the constrained nodes in force balanced models of the femur. In particular three different load cases were considered in this study (Figure 1.9, top):

- a. All of the joint and muscle forces from the musculoskeletal model formed a *complex set*;
- b. A simplified load case including a hip contact and abductor force;
- c. The case *b* additionally including the vastus lateralis, medialis and intermedius muscle forces.

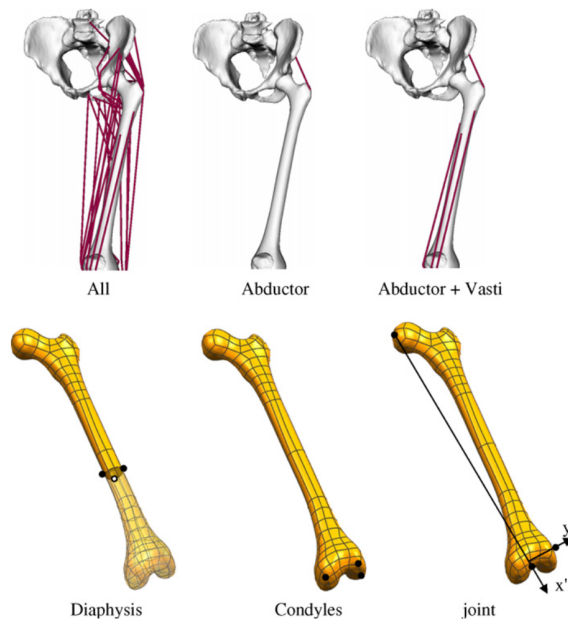


Figure 1.9: Top: muscle sets included in the analysis. Bottom: oblique view of the femur solid model showing the location of node constraints for each configuration. [17].

While regarding the BCs, three methods were considered for preventing rigid body motion by applying displacement constraints at three nodes (Figure 1.9, bottom):

- a. All three nodes were fully constrained at the mid-diaphysis part of the femur.
- b. All three nodes were fully constrained at distal condyles of the femur.
- c. A node in the center of the knee was limited in three translational degrees of freedom (DOF). The node at the hip contact position, where the hip contact force was applied, was constrained in two degrees of freedom, allowing it to bend only along an axis towards the center of the knee. The sixth DOF was constrained at a node on the distal lateral epicondyle to prevent anteroposterior movement, effectively inhibiting rotation of the model's rigid body around the hip-knee axis.

These methods and load conditions were used in combination in 5 different studying cases: (A) diaphyseally constrained with hip contact and abductor forces; (B) case A plus vasti forces; (C) case A with complete set of muscle forces; (D) distally constrained with all muscle forces; (E) physiological constraints with all muscle forces. For the first time, a method has been proposed for constraining the femur in numerical models, allowing for physiological deflection of the femoral head under complex loading conditions. The application of nonphysiological constraints resulted in nonphysiological deflections and altered stress patterns on the femur. Only by applying physiologic constraints was it possible to reproduce physiological deflections under difficult loading conditions. This approach will not only influence the results of finite element studies by providing a standardized method for constraining models, but it may also serve as a benchmark for studying all long bones in the body.

Chapter 2

Material and methods

In this chapter there will be an analysis of how the multibody model was implemented and what parameters were chosen in order to obtain muscle and joint reaction forces. Following a section explaining the calculation that was used to obtain resultant forces and moments. The process of transferring the joint and muscle forces to the FE model, in addition to the appropriate FE parameters selected, will be discussed in the final section.

2.1 Implementation of Multibody model

Muscle and joint contact forces were calculated for a static pose using a simplified musculoskeletal model from OpenSim's [9] default folder. In particular, starting from '*Gait2392.osim*' model [18], it was scaled to match the experimental data of the a subject with body weight of 750 N and it was simplified by reducing the number of muscles that were directly in contact with the femur of the right leg (Figure 2.1). More specifically, 12 muscles were selected and listed in the Table 2.1. The maximum isometric forces (MIF) of the twelve selected muscles were also listed. The choice of the 12 selected muscles was made in order to reduce the complexity of the model, selecting a significant representation of the muscles directly in contact with the femur. In particular, the muscles with a higher force contribution for each muscle group were selected.

The global coordinate system was set as shown in the figure 2.1, in particular, the antero-posterior axis (X-axis) was defined with its positive direction pointing towards the anterior aspect, representing the front of the subject, while the negative direction extends towards the posterior. Concurrently, the longitudinal axis (Y-axis) was aligned with the positive direction directed towards the head of the subject, emphasizing cephalic orientation, and the negative direction extending towards the feet, indicative of a caudal position. Lastly, the medio-lateral axis (Z-axis)

completes the triad, where the positive direction was extended laterally, marking the side of the subject, and the negative direction was converged medially, signifying the central aspect.

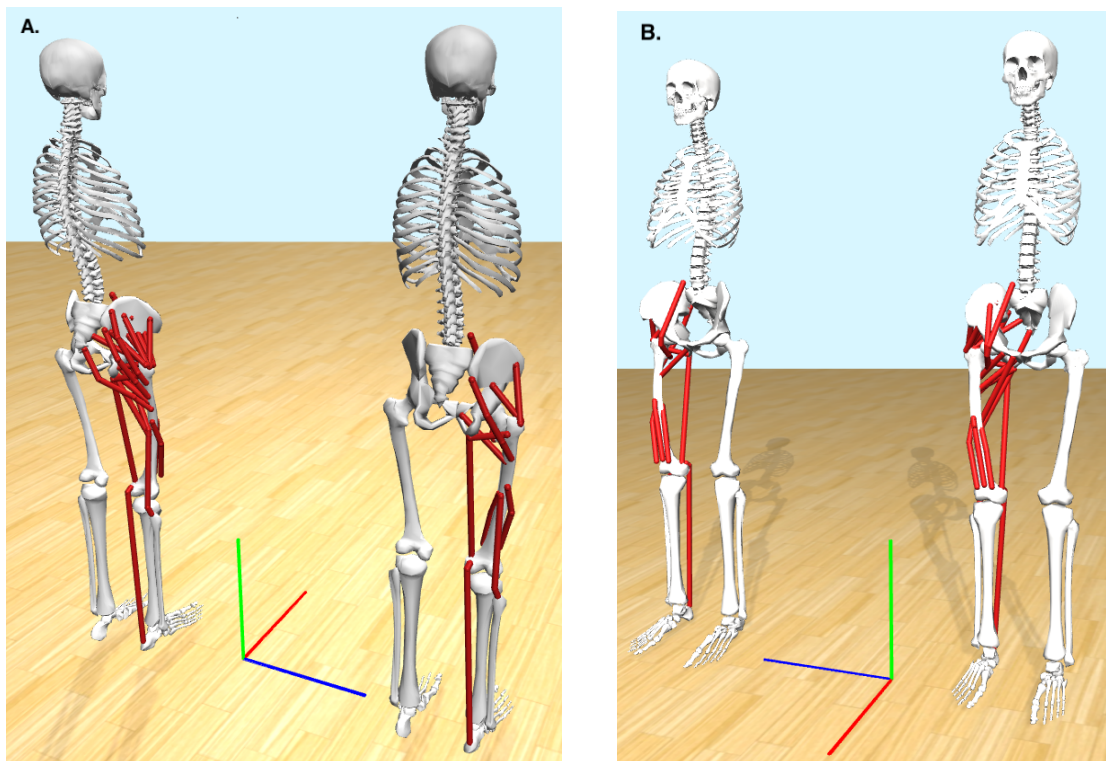


Figure 2.1: Representation of muscles that were directly in contact with the femur. Global coordinate system: X(Red), Y(Green), Z(Blue). (A.) On the left, the complete model with all muscles. On the right the same model but with the selected twelve muscles. (B.) On the right, the complete model with all muscles. On the left the same model but with the selected twelve muscles.

The femoral head becomes the centre of the local coordinate system used in all of the data that were subsequently obtained (Figure 2.2).

Muscle	MIF
Glu med1	819 N
Glu min3	323 N
Bifemsh	804 N
Add brev	429 N
Add mag3	488 N
Glu max2	819 N
Psoas	1113 N
Quad fem	381 N
Vas med	1294 N
Vas int	1365 N
Vas lat	1871 N
Med gas	1558 N

Table 2.1: The twelve selected muscles with their relative maximum isometric force (MIF) that the fiber can generate.



Figure 2.2: Local coordinate system. X(Red), Y(Green), Z(Blue)

2.1.1 Muscle and Joint Reaction forces calculation

The analysis concentrated on a static trial, specifically gathering data from a subject in a static pose. Consequently, the marker set applied to anatomical points remained relatively consistent with the initial position throughout the trial. The collected data served as input for OpenSim’s Static Optimization tool. This tool was employed to estimate muscle forces by minimizing the sum of squared muscle activations for each frame in the kinematic data, while respecting to constraints such as joint moment equilibrium and physiological limits for muscle forces. Finally, joint contact forces (JCFs) were calculated at the hip and the knee joint.

All musculoskeletal simulations were performed in OpenSim [9]. All loads acting on the femur were determined with respect to the segment reference system in order to be applied to the FE model. The inertial load and the gravitational force were calculated at the thigh centre of mass based on the segment kinetics, the joint contact forces were calculated at the joint centres using the *JointReactionAnalysis* tool available in OpenSim [19], while the femoral attachment point coordinates of each muscle actuator, together with the direction and magnitude of the muscle force, were extracted using the plugin, *MuscleDirectionForce*, developed by the authors Van Arkel et al. [20].

In the following analyses, a single frame from the full cinematic recording was examined. Every frame was selectable because the analysis in question was performed on a subject in a static pose.

2.1.2 Resultant Forces and Moments calculation

All the data acquired from OpenSim (Figure 2.3) were utilized in a in-house MATLAB [21] script in order to calculate the resultant force and moment acting on the femur.

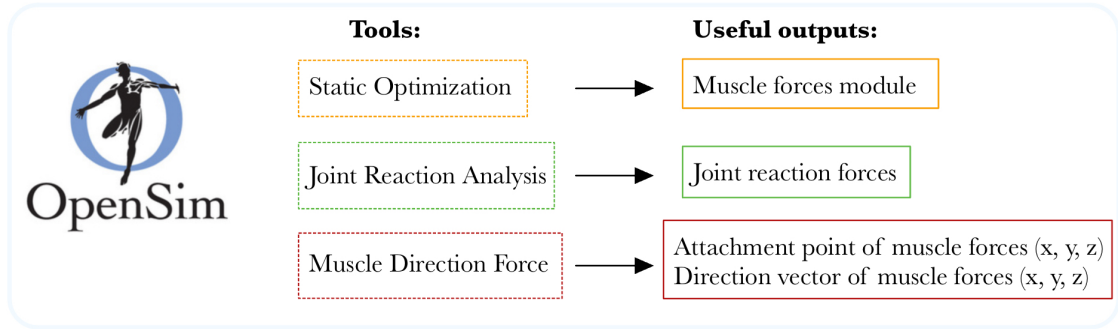


Figure 2.3: Output from OpenSim utilized in the MATLAB script.

Specifically, the following formula provides the resultant forces' calculation:

$$F_{\text{res}}(x, y, z) = F_g + F_{\text{hip}}(x, y, z) + F_{\text{knee}}(x, y, z) + \sum_{i=1}^n |F(i)| \cdot \frac{v_{\text{dir}}(x_i, y_i, z_i)}{\|v_{\text{dir}}(x_i, y_i, z_i)\|}$$

Where $F_{\text{res}}(x, y, z)$ represents the resultant force vector, $|F(i)|$ represents the module of i th muscle force and $\|v_{\text{dir}}(x_i, y_i, z_i)\|$ represents the norm of the direction vector of the i th muscle force. While n represents the number of muscle forces. The first two terms, respectively $F_{\text{hip}}(x, y, z)$ and $F_{\text{knee}}(x, y, z)$, represent the contribute of joint reaction forces. Finally, F_g , which is the femur's weight, was used in this calculation.

The following formula explains how to determine the resultant moment:

$$M_{\text{res}} = M_{\text{hip}}(x, y, z) + M_{\text{knee}}(x, y, z) + \sum_{i=1}^n (|F(i)| \cdot \|v_{\text{dir}}(x_i, y_i, z_i)\| \times r(x_i, y_i, z_i))$$

Where $M_{\text{res}}(x, y, z)$ represents the resultant moment of all the muscle forces in relation to the centre of the reference system, the femoral head, plus $M_{\text{hip}}(x, y, z)$ and $M_{\text{knee}}(x, y, z)$, that represent the moment referred to the head of the femur by the joint reaction forces.

Verifying that all the forces acting on the femur are in equilibrium with each other is crucial for the simulations with the FE model to converge towards a solution. Therefore it is necessary to verify that the result of the forces applied to the femur is theoretically zero, or at least is as close as possible to zero. For this reason these calculations were done.

2.2 FE model: Boundary and Load conditions

From the geometry file extracted from OpenSim [9], *femur_r.vtp*, Ansys® ICEM CFD was used to create a mesh of the femur with 287,548 elements. In particular, SOLID187 (from Ansys® element library) was used as element. The mesh was exported as an Ansys® MAPDL (ANSYS Mechanical APDL, Ansys Inc., PA, USA) input file, *MeshedFemur.cdb*. In order to simplify the simulation one material property was chosen for the femur, in particular the young modulus of the cortical bone was chosen ($E=17,000\text{MPa}$) and the Poisson coefficient was set to $\nu=0.33$, as reported in the study of Duda et al. [13]. The purpose of the FE analysis was to evaluate the deformations on the external surface of the femur, subjected to muscle forces.



Figure 2.4: Load condition for the *reference case*: load force applied to the centre of femoral head (green arrow).

For FE analysis an in-house MAPDL code was used in order to apply certain conditions. In particular, all the cases were analyzed in the FE model simulating a fall on the side. A concentrated point load of 1kN was applied at the centre of the

femoral head. The diaphysis nodes were linked to the knee centre, modelled as a hinge, through beams elements. At the greater trochanter, a non-linear surface-to-surface contact using augmented-Lagrange algorithm was employed, where the surface area of the greater trochanter was in contact with an infinitely rigid plane. These information were reported in detail in the case studies of Bhattacharya et al.[22], Altai et al.[23] and Aldieri et al.[24]. A simulation was launched with the model containing the conditions mentioned above, with the hinge at the center of the knee linked to the diaphysis nodes serving as boundary condition and the loading force applied at the centre of the femoral head as the loading condition (Figure 2.4). This became the *reference case*, allowing for comparison with other cases involving muscle forces and varying boundary conditions.

In this thesis study, five simulation cases were analysed. Every muscle force derived from OpenSim was applied for each case study in addition to the force load (Figure 2.5); in particular, muscle forces were applied to the node closest to the OpenSim-determined muscle attachment points. What differentiates the various cases were the constraints applied to the FE model, choosing them in reference to previous studies, which were analyzed in the introduction. The five cases are summarized in Table 2.2.

Cases	Constraints	Authors
0	Diaphysis nodes linked to hinge node at the knee	Altai et al.[23]
1	Distally fully constrained	Altai et al.[5], Martelli[15]
2	Three nodes fully constrained at mid-diaphysis	Speirs et al.[17]
3	Three nodes with specific constraints at distal end	Altai et al.[5]
4	Physiological constraints	Speirs et al.[17]

Table 2.2: Simulation cases.

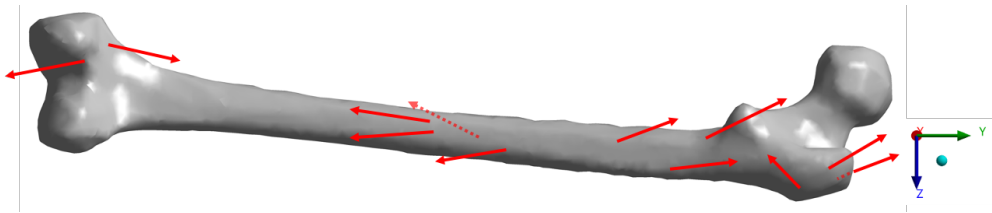


Figure 2.5: Load condition for all the cases except for the reference case. Muscle forces applied to the FE model surface (red arrows). For all the muscle forces, the three component (x,y,z) were considered. Load force applied to the centre of femoral head (green arrow).

2.2.1 Simulation cases

The boundary conditions for the case 0 were the same boundary conditions of the *reference case* [22][23][24], where the diaphysis nodes were linked to the knee centre, modelled as a hinge, through beams elements (Figure 2.6). All the muscle forces were applied on the surface of the femur in addition to the force load applied in the centre of the femoral head.

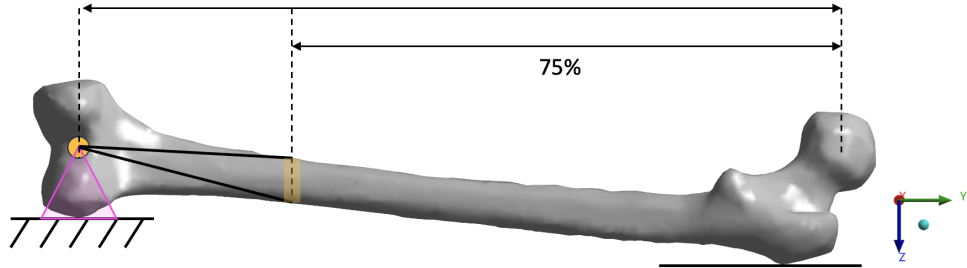


Figure 2.6: Boundary conditions for case 0: hinge at the knee node (in orange) linked to a selection of diaphysis nodes through beams elements (in black). Black arrows represent biomechanical length [22][23][24].

The Altai et al. [5] and Martelli [15] studies provide the reference resources for the case 1. As highlighted in the first chapter, these studies had set a determined condition, that represents the most constrained condition that can produce the highest reaction forces [5]. Using Ansys® MAPDL, the same constraints were set on the studying FE model. The nodes in the distal part of the femur were all selected (Figure 2.7). The displacements of the selected nodes were constrained in all the directions.

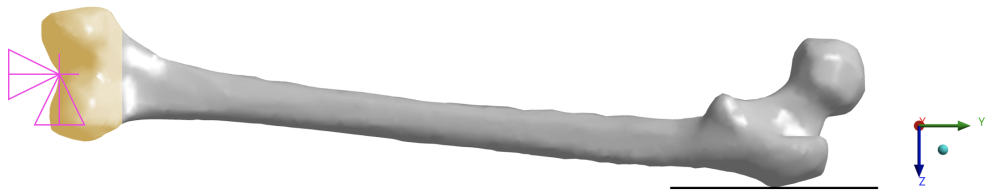


Figure 2.7: Boundary conditions for Case 1: all the nodes (selection in yellow) in the distal portion of the femur were fully constrained (in pink) [5][15].

Similar to the case 1, with the difference that in this second case only three nodes were fully constrained in the mid-diaphysis of the femur. This condition was shown in the study of Speirs et al. [17]. In order to simulate this instance with Ansys®

MAPDL, a few nodes were chosen from the femur's mid-diaphysis. Subsequently, only three nodes of that selection were constrained along all directions. (Figure 2.8).

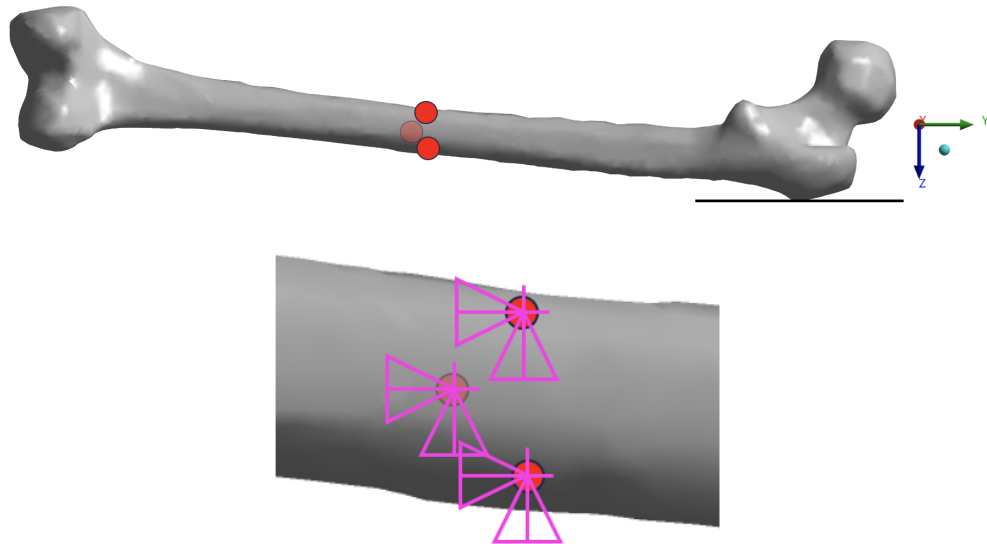


Figure 2.8: Boundary conditions for Case 2: three selected nodes from the femur's mid-diaphysis are shown in the top image (in red); the three selected nodes were fully constrained (in pink), shown in the bottom image [17].

In the case 3 was replicated the conditions shown in the study Altai et al. [5]. In particular, three nodes were chosen as more relaxed BCs:

1. The most distal node of the medial condyle was fully constrained.
2. The most distal node at the lateral condyle was constrained in along X and Y displacements.
3. One node near the patella groove was constrained along X displacements.

Three zones in the distal portion of the femur were chosen using Ansys® MAPDL, each of them close to the corresponding node to be chosen. For the zone of the medial condyle, a distal node was chosen searching for the nodes with the minimum value of the Y component. The same operation was done for the distal lateral zone and the zone of the patella groove. In the figure 2.9 were shown the three selected nodes with the respective constraint conditions.

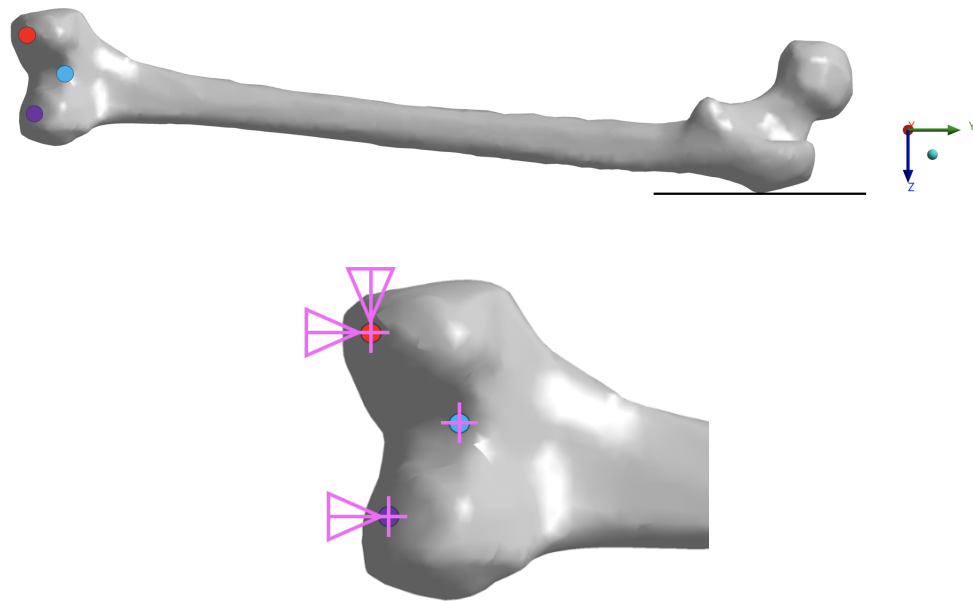


Figure 2.9: Boundary conditions for Case 3. Three selected nodes: in purple the most distal node at the lateral condyle, in red the most distal node of the medial condyle and in blue the patella groove node in the top image. The most lateral node (purple) was constrained in X and Y displacements, the most medial node (red) was fully constrained and the patella groove node (blue) was constrained in X displacements, shown in the bottom image [5].

For the case 4, Speirs et al.'s [17] article was used as reference. In that study node constraints were selected to approximate physiological constraints at the knee and hip, precisely:

1. The node on the femoral head's surface, referred to as the hip contact node, was constrained in X and Y displacements.
2. One node near the patella groove was fully constrained.
3. A node on the distal lateral epicondyle was constrained in X displacement.

Ansys® MAPDL was used to select three zones on the femur surface, each of that was close to the corresponding node that was required to be selected. In the figure 2.10 was shown the three nodes selected: the hip contact node was chosen by starting at the head femoral node and looking for the node that had the lowest values for the Z and Y components; while the distal lateral epicondyle node was chosen by starting by the knee centre node and searching the node with the maximum value for the Z component (z). The respective constrained was shown in

the figure 2.11.

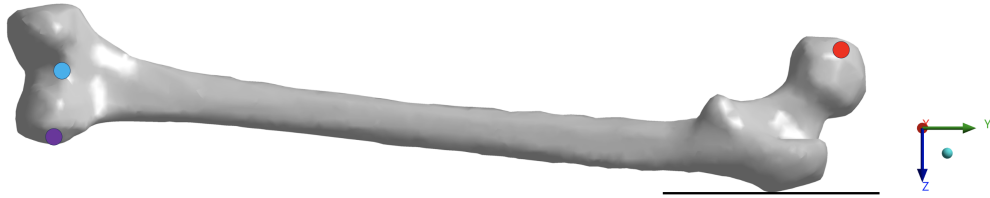


Figure 2.10: Boundary conditions for Case 4: Three nodes selected: node on the femoral head's surface, referred to as the hip contact node (red), a node on the distal lateral epicondyle (purple) and one node near the patella groove (blue).

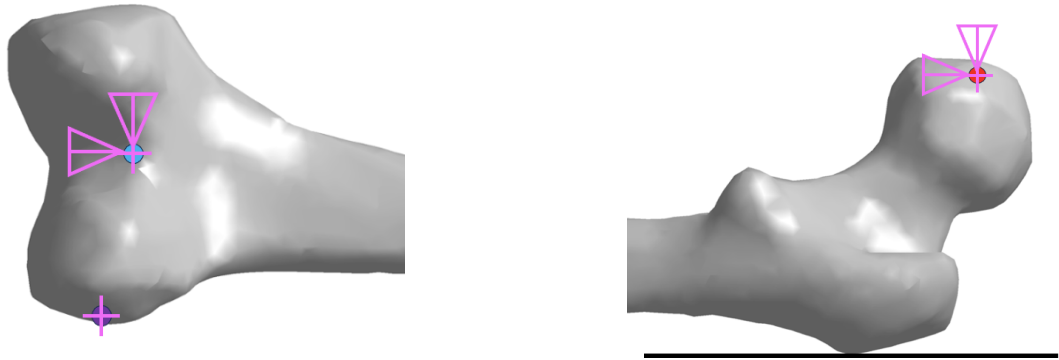


Figure 2.11: On the left: the node on the distal lateral epicondyle was constrained in X displacement and the node near the patella groove was fully constrained. On the right: The node on the femoral head's surface, referred to as the hip contact node, was constrained in X and Y displacements [17].

Chapter 3

Results and discussion

This chapter provides a comprehensive review of the mechanical results obtained for each case in a specific region of interest under different boundary conditions. This chapter examines the principal strains (ϵ_1 and ϵ_3), providing insights into their distribution and statistical significance.

The analysis begins with a description of the region of interest, as well as the data collection and analysis methods. The results are then presented, including average and standard deviation (SD) calculations for the principal strains.

3.1 Analysis of Principal Strains

The findings from the analysis of principal strains (ϵ_1 and ϵ_3) in a specific region of interest (Figure 3.1) were investigated. This region includes the proximal part of the femur, the lateral portion of the greater trochanter is not included in the selection process because of the boundary conditions effect. All external nodes in this area were chosen, and the data linked to the principal strains of these nodes represented the distribution of the data used in the following analyses.

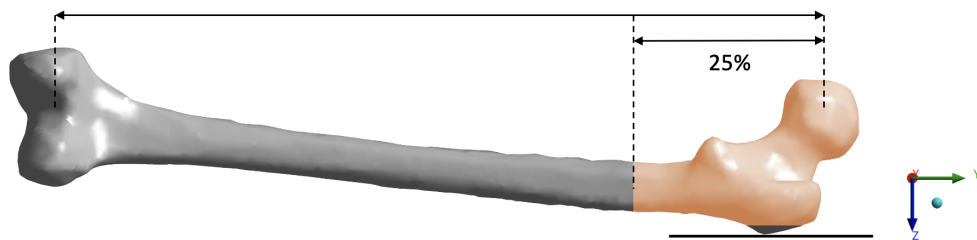


Figure 3.1: Region of interest for the analysis of the results. The lateral part of the greater trochanter is excluded due to boundary conditions effect, with the biomechanical length indicated by the black arrow.

The analysis focused on the maximum and minimum strains, with mean and standard deviation calculations performed for each case, where the average values represent the central tendency of the principal strains for each case, while the standard deviations (SD) represent the dispersion or variability of the principal strains around the mean value for each case. These values are summarized in the tables (3.1 and 3.2), which shows that the average value of the principal strains for all cases is similar to the average value of the reference case, in which muscle forces were not considered.

Table 3.1: Strain Mean and Standard Deviation of maximum strains (ϵ_1).

Case	Mean ϵ_1 (%)	SD ϵ_1 (%)
Reference case	0.248	± 0.333
Case 0	0.247	± 0.343
Case 1	0.248	± 0.341
Case 2	0.232	± 0.313
Case 3	0.285	± 0.390
Case 4	0.085	± 0.207

Table 3.2: Strain Mean and Standard Deviation of minimum strains (ϵ_3).

Case	Mean ϵ_3 (%)	SD ϵ_3 (%)
Reference case	-0.253	± 0.335
Case 0	-0.253	± 0.346
Case 1	-0.254	± 0.343
Case 2	-0.238	± 0.313
Case 3	-0.290	± 0.392
Case 4	-0.087	± 0.130

Maximum strains with applied muscle forces show average values ranging from 0.085% to 0.285%. The reference case without muscle forces has an average value of approximately 0.248%. For minimum principal strains, applied muscle forces produce average values ranging from -0.087% to -0.290%. Instead, the reference case without muscle forces show an average value of approximately -0.253%. For the cases with applied muscle forces, the SD values vary among cases but generally range from approximately 0.207% to 0.390% for the maximum principal strains and from approximately 0.130% to 0.392% for the minimum principal strains. The case without muscle forces has slightly lower SD values, ranging from approximately 0.333% to 0.335% for the maximum and minimum principal strains, respectively.

Case 3 has the highest average strain value (0.285%). However, it is consistent with the average values of previous cases. This case has also the highest standard deviation ($\pm 0.390\%$), as shown in the table (3.1). Case 3 has the highest average minimum strain value, 0.290% (modulus), with an SD value of $\pm 0.392\%$, which is similar to the SD value for maximum strains.

However, the strains' mean values differ minimal between cases within the analyzed region of interest. This suggests that the inclusion of muscular contributions and variations in boundary conditions may not have a significant impact on causing important variations in the various simulations performed. Despite the addition of muscle forces and changes in boundary conditions between cases, average strain values remain relatively stable. This implies that other factors, rather than the specific conditions under investigation, may have a greater impact on the mechanical response of the system.

An analysis of the contour plots generated by Ansys APDL will provide visual confirmation of the above observations. In addition, the findings will be supported by a statistical analysis using histograms and distributions in the following sections. Nonetheless, the consistency in mean strain values across simulations provides useful information about the model and the region's relative insensitivity to changes in muscle forces and boundary conditions.

3.2 Visual and Statistical Analysis

For a deeper understanding of the data, contour plots were generated to visualize the distribution of strains in different cases. Subsequently, the focus shifted to the region of interest to visually compare differences between cases.

The contour plots of the principal strains of the entire femur, highlight the various boundary conditions used in the five study cases. For both the distribution of $\epsilon 1$ and $\epsilon 3$, the color map varies only in the distal part, where the constraint conditions have changed. In fact, case 3, with only three nodes constrained in the distal part, has higher deformation values than the others in this area. The other cases, which have more restrictive constraint conditions, have lower deformations in the distal part than case 3. Although case 2 has three constrained nodes, like case 3, the deformations in the distal part of the femur are comparable to cases where a selected group of nodes are constrained, as in cases 0 and 1. This is because the three constrained nodes in case 2 were chosen in the mid-diaphysis region.

Although the differences between the various cases in the distal part are minor, they do not exist in the proximal part, which is the focus of this thesis's case study. In other words, the distribution of principal strains in the region of interest remains largely unchanged for both $\epsilon 1$ and $\epsilon 3$. Figures 3.2 and 3.3 show an isometric view of the femur region of interest, along with the corresponding contour plots of $\epsilon 1$ and $\epsilon 3$.

These figures demonstrate how the distribution of principal strains remains largely unchanged. Figure 3.2 shows that the areas with the highest values, highlighted in red, are the same in all cases. The same situation occurs for the minimum values in figure 3.3, showing the ϵ_3 strains, in which the areas with the minimum values are substantially the same.

First principal strain distribution

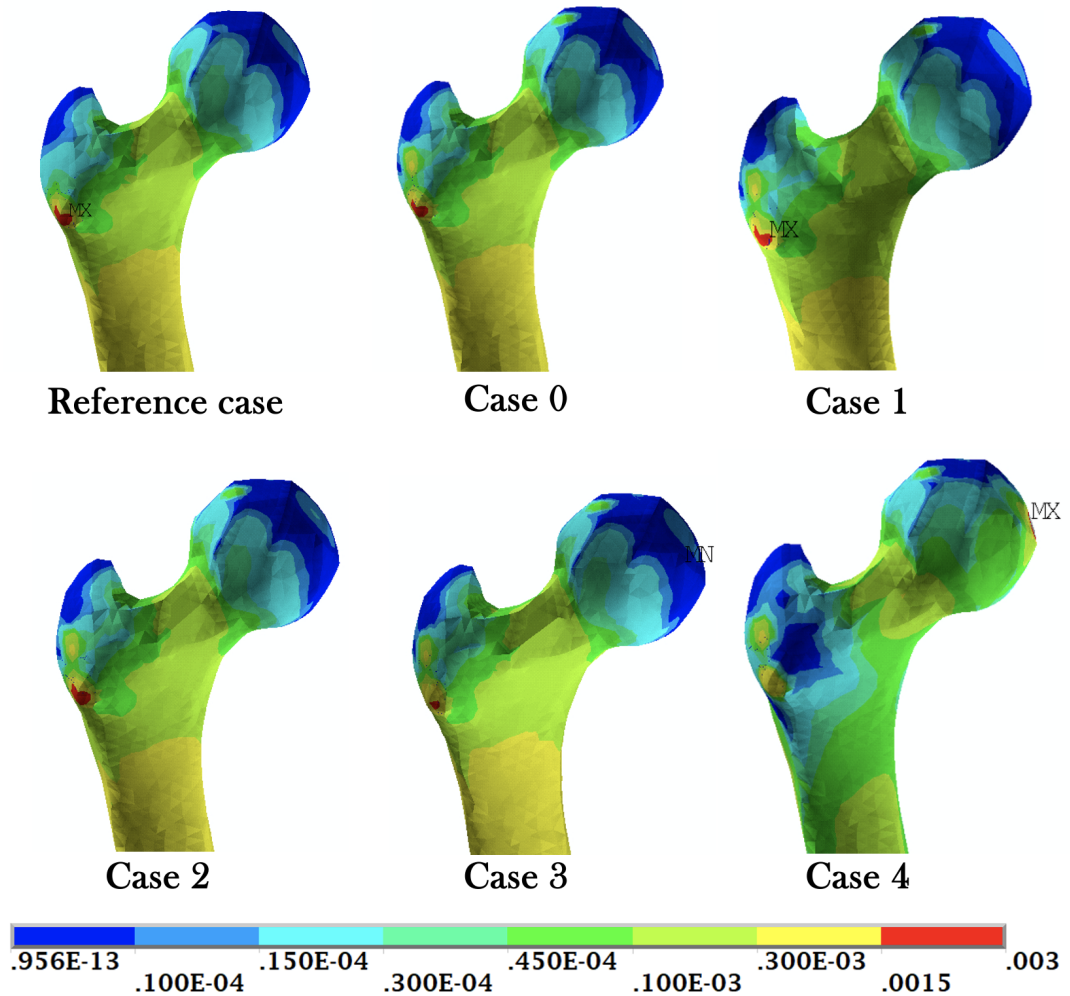


Figure 3.2: Maximum strains distribution within the region of interest. Strains are shown for all the cases. It is shown the isometric view of the femur.

Case 4 stands apart from the others. As expected, the strain distribution in the proximal part differs from previous cases due to the constraint condition imposed there. This condition is highlighted in figures 3.2, and 3.3. Figures 3.2, and 3.3

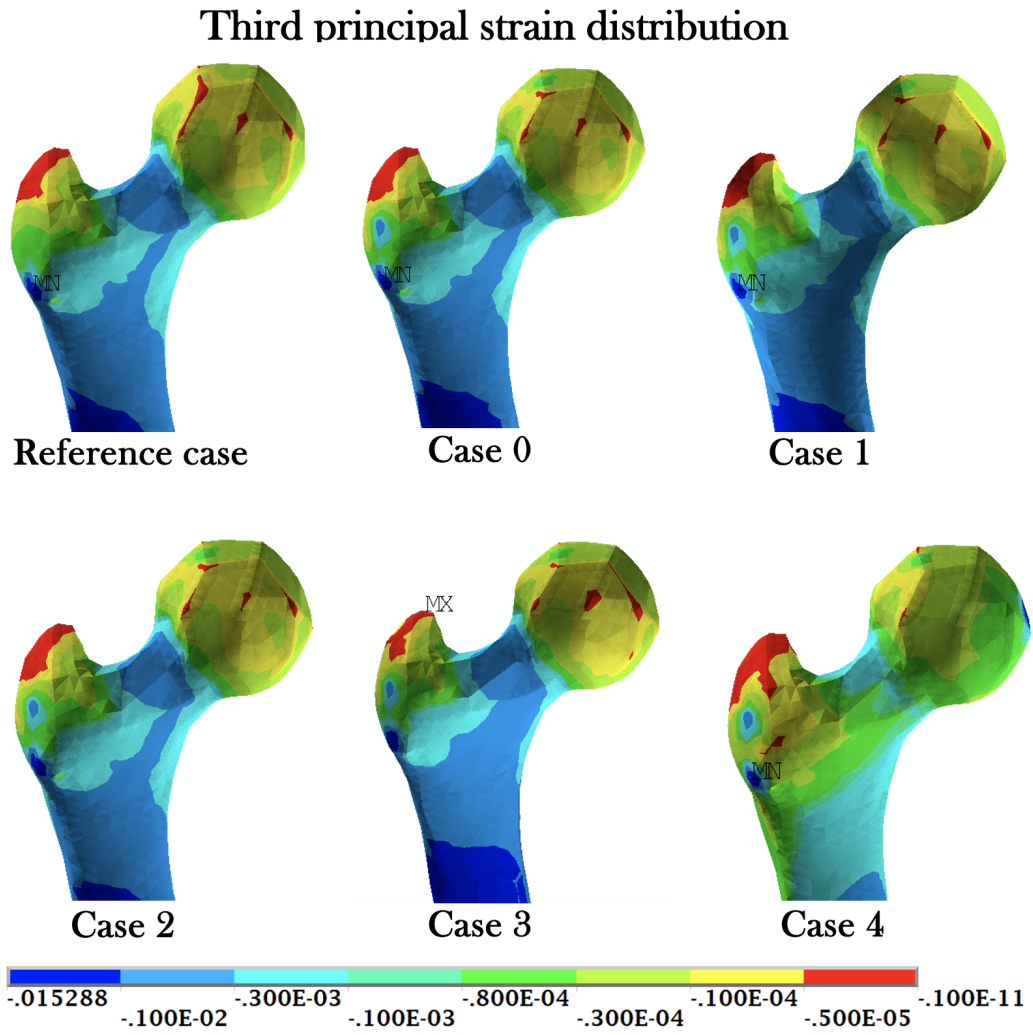


Figure 3.3: Minimum strains distribution within the region of interest. Strains are shown for all the cases. It is shown the isometric view of the femur.

demonstrate how the distribution of case 4 differs from the other cases, with minor strains for both ϵ_1 and ϵ_3 .

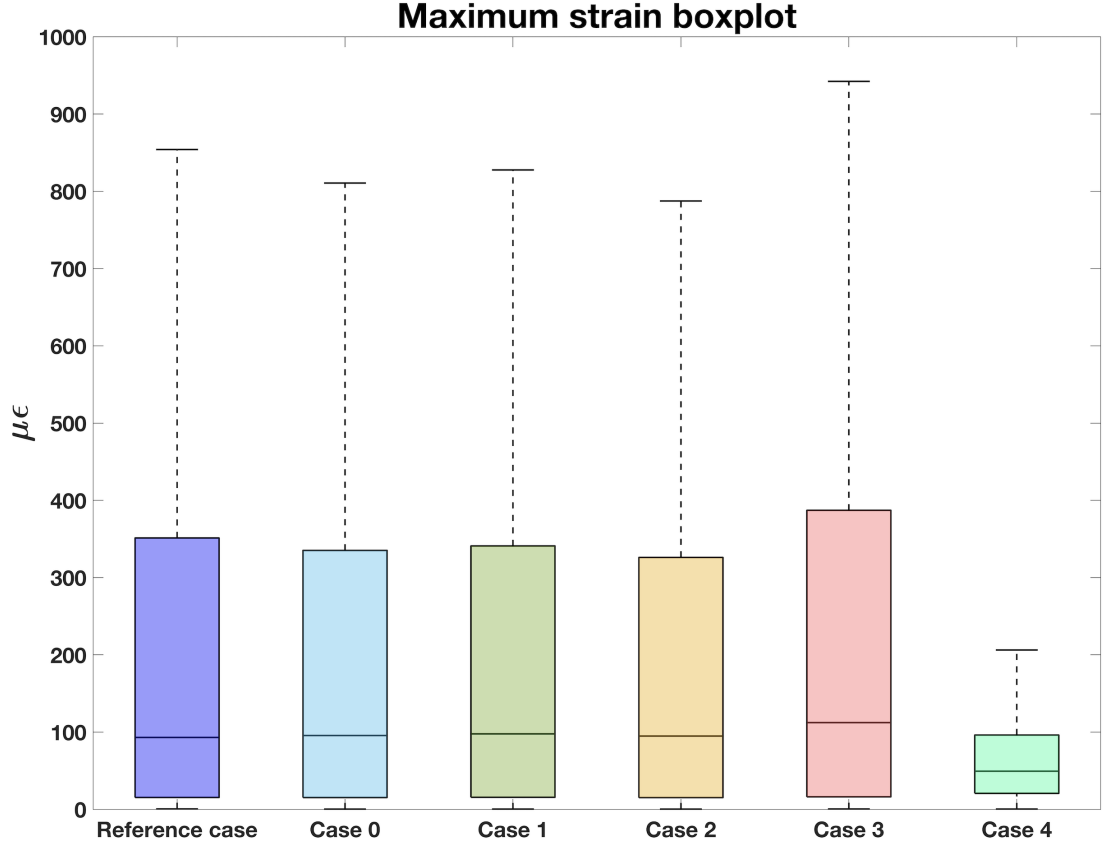


Figure 3.4: Comparison of strain distributions in various cases. The reference case is shown in purple, with the other five cases in the following order: blue, green, yellow, red, and aquamarine. The figure shows the boxplots of the maximum strains (ϵ_1).

The visualization of results using contour plots allows for an immediate comparison of the various cases, highlighting the regions subject to the greatest deformations. Boxplots were used to obtain a visual distribution of the data within each case (Figures 3.4 and 3.5), allowing for an immediate evaluation of the data's variability and dispersion. Figure 3.4, which shows the maximum deformation values of the various cases, shows that the data distributions are similar across the cases. In particular, 75% of the deformations assume values less than $500 \mu\epsilon$ in all cases, with peak values exceeding $800 \mu\epsilon$.

The median value is closer to the first quartile, indicating that the majority of the data is concentrated at the lower end of the distribution. This indicates that the

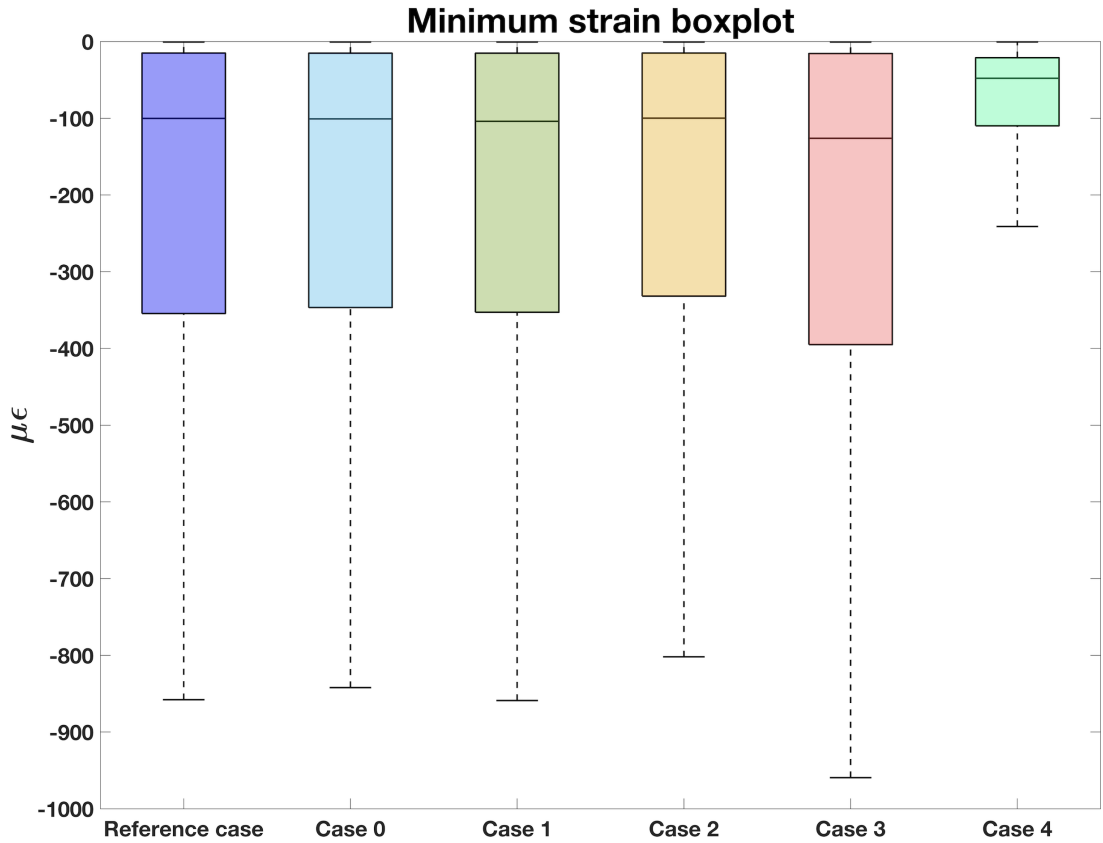


Figure 3.5: Comparison of strain distributions in various cases. The reference case is shown in purple, with the other five cases in the following order: blue, green, yellow, red, and aquamarine. The figure shows the boxplots of the minimum strains (ϵ_3).

data distribution is asymmetric, with a longer tail pointing to higher deformation values. The majority of the deformations are on the order of hundreds of $\mu\epsilon$, and the median value supports this trend. There are no important variations between the various cases, and their distributions are similar. In particular, cases where muscular forces act on the femur result in a strain distribution similar to that produced in the reference case, where muscular forces are not applied. The imposed boundary conditions did not result in important variations in the strain distributions. However, this argument changes only for case 4, which confirms a different distribution compared to the other case studies, precisely because it presents the boundary condition in the proximal part. Therefore, as expected, the distribution of the data differs from the other cases, showing lower deformation values and low variability.

The analysis performed on the maximum strains is also applicable to the minimum

strains. Figure 3.5 shows a boxplot for the minimum strains, with all values being negative, indicating a general compressive stress on the surface.

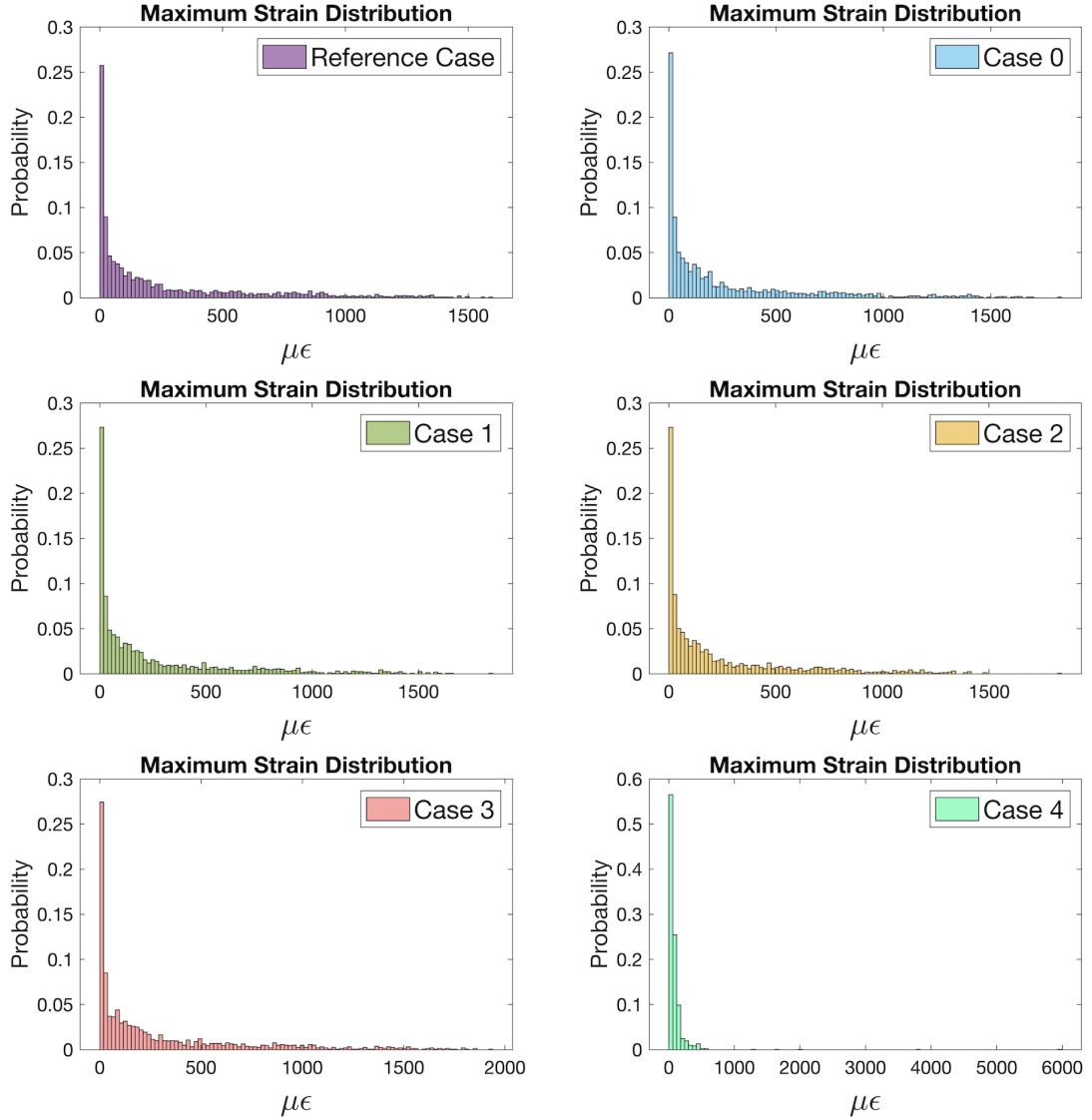


Figure 3.6: Comparison of strain distributions in various cases. The reference case is shown in purple, with the other five cases in the following order: blue, green, yellow, red, and aquamarine. The figure shows the histograms of the maximum strains (ϵ_1).

To investigate the consistency of the observed results across different cases, a more detailed analysis was performed using histograms and distribution curve fittings. This allowed for a more in-depth examination of the data distribution

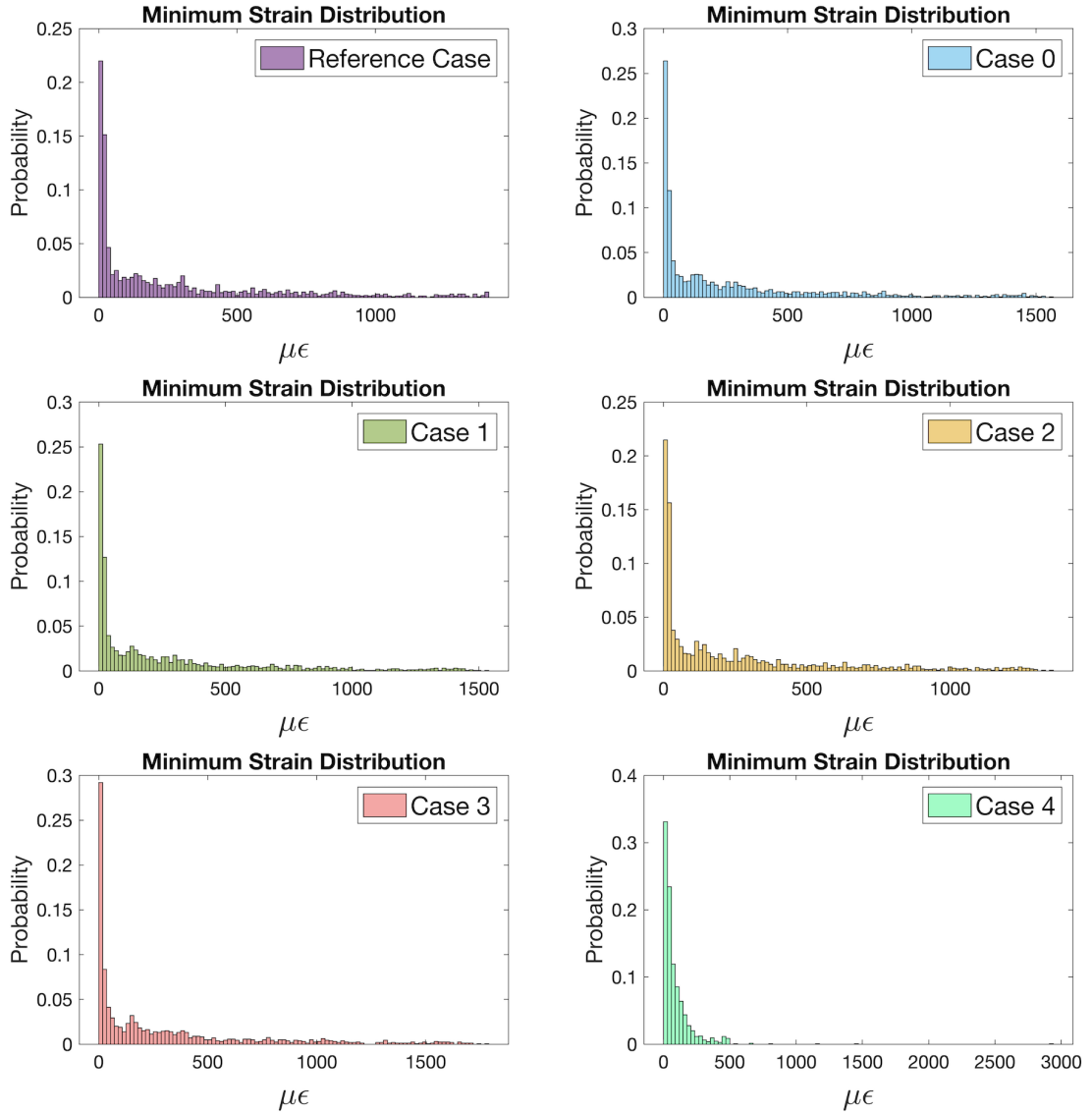


Figure 3.7: Comparison of strain distributions in various scenarios. The reference case is shown in purple, and the other five cases are in the following order: blue, green, yellow, red, and aquamarine. The figure depicts the histograms of the minimum strains (ϵ_3). The absolute value of the data was taken.

within each case, as well as comparisons of distribution characteristics. After generating histograms of deformation data for each case, a significant similarity in distribution shapes was discovered (Figures 3.6 and 3.7). A consistent trend towards lower deformation values is observed across all cases, as evidenced by the fact that the majority of the high-frequency bins are located at the beginning of

the graph. The y-axis represents the Probability and the x-axis represents the $\mu\epsilon$ values in both figures.

The distribution of strains is not symmetric, as expected from the boxplot analysis. Indeed, the majority of strains occur at low deformation values and are concentrated in the first part of the histogram, with few in the latter part of the graph, highlighting a long right tail. The distribution shape is the same for maximum and minimum strains, as shown in the figures 3.6 and 3.7.

The fitting distribution process was used to better identify and understand the structure and characteristics of the data distribution, as well as generate parameter estimates for modeling. Experimentally, the gamma model was chosen to describe the data distribution because it was considered the most appropriate among those considered. The gamma distribution is commonly used when data has a positively skewed distribution with a longer tail towards higher values, as in the observed cases. To visually assess and directly compare the analyzed deformation data to the selected theoretical model, both maximum strains (ϵ_1) and minimum strains (ϵ_3) were displayed in the same figure, 3.8 and 3.9 respectively. The y-axis in both graphs represents the probability density function (PDF), while the x-axis plots $\mu\epsilon$ values. The figures clearly show that the observed data distribution is consistent with the gamma model, confirming that the model accurately captures how the data is organized.

After analyzing the histograms with the fitted distributions, we will use the Kolmogorov-Smirnov test to compare the study cases to the reference case. This statistical test evaluates the similarity between the distributions of the principal strains (ϵ_1 and ϵ_3) and their fitted distributions. The obtained p-values provide information on the degree of agreement between each study case and the reference case, as well as the effectiveness of the applied muscle forces and boundary conditions in influencing strain distribution patterns.

The tables 3.3, 3.4, 3.5, 3.6 report the p-values obtained from the Kolmogorov-Smirnov (KS) test used to compare the data distributions between the reference case and the other cases in tables 3.3 and 3.5, and the Case 0 with the study cases 1, 2, 3, and 4 (in tables 3.4 and 3.6) for both the maximum strains (ϵ_1) and the minimum strains (ϵ_3), as well as the data obtained from the distribution fitting. The tables show that, for both the maximum strains (ϵ_1) and the minimum strains (ϵ_3), the p-values are generally high, indicating significant similarity between the distributions of the study cases and the reference case. This suggests that the study cases do not show significant differences compared to the reference case regarding the strains distribution. Also tables 3.4 and 3.6 show that there are no significant differences between Case 0 and the other cases with varying boundary conditions. As expected, the case with constraints on the proximal part (Case 4) showed a significantly low p-value compared to the other cases, as it presents limitations that affect the distribution of strains. This result was predictable and confirms

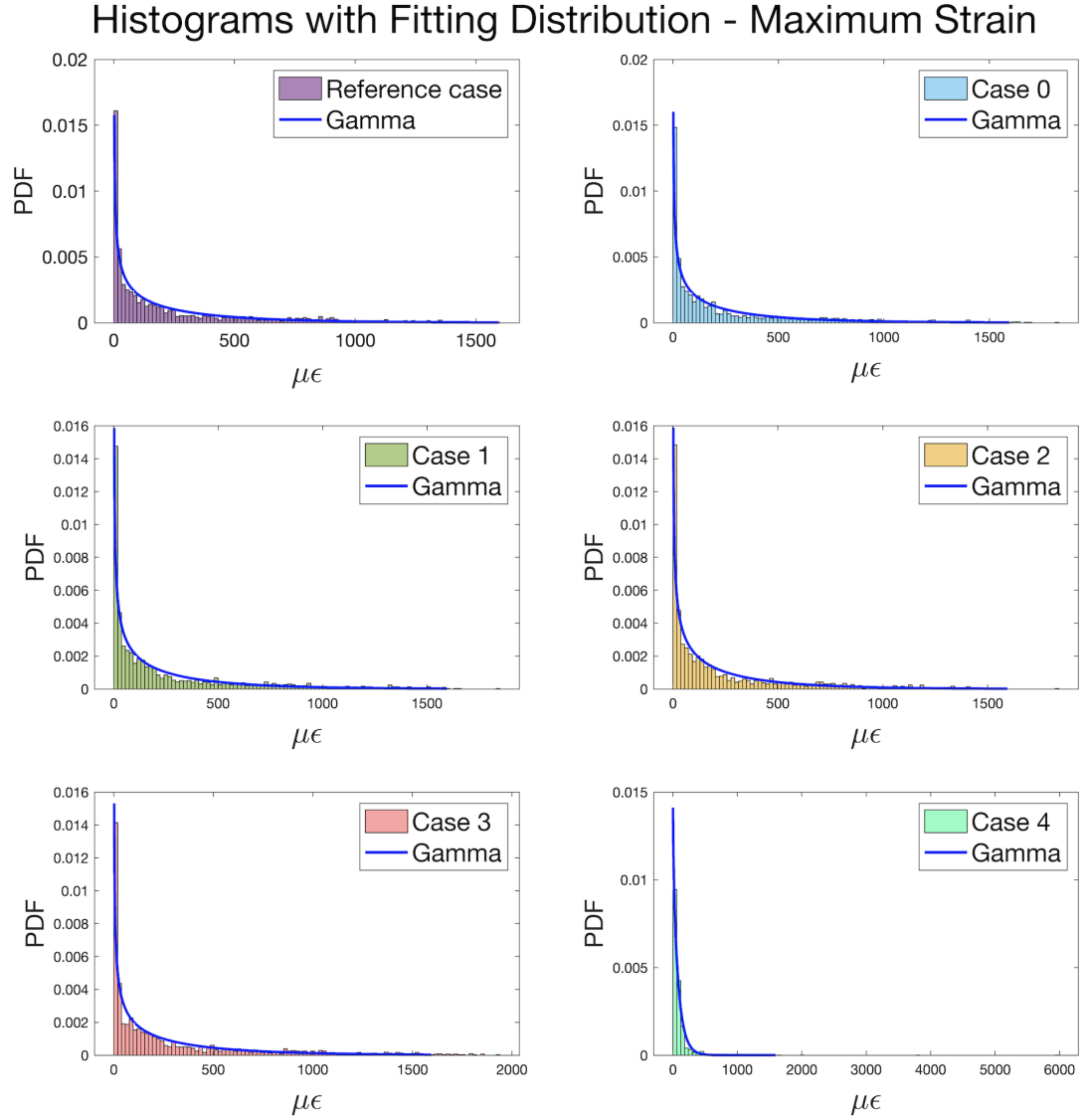


Figure 3.8: Histograms of deformation data overlaid with fitted gamma distribution curves. The y-axis represents the probability density function (PDF), while the x-axis shows $\mu\epsilon$ values. The fitted curves closely match the observed data distribution for maximum strains (ϵ_1) across all analyzed cases.

the validity of the model. For example, for the maximum strains (ϵ_1) in Case 4, the p-value is very low (0.003), suggesting that the strains distribution in this case may be significantly different from the reference case. The same is observed for the minimum strains (ϵ_3) in Case 4.

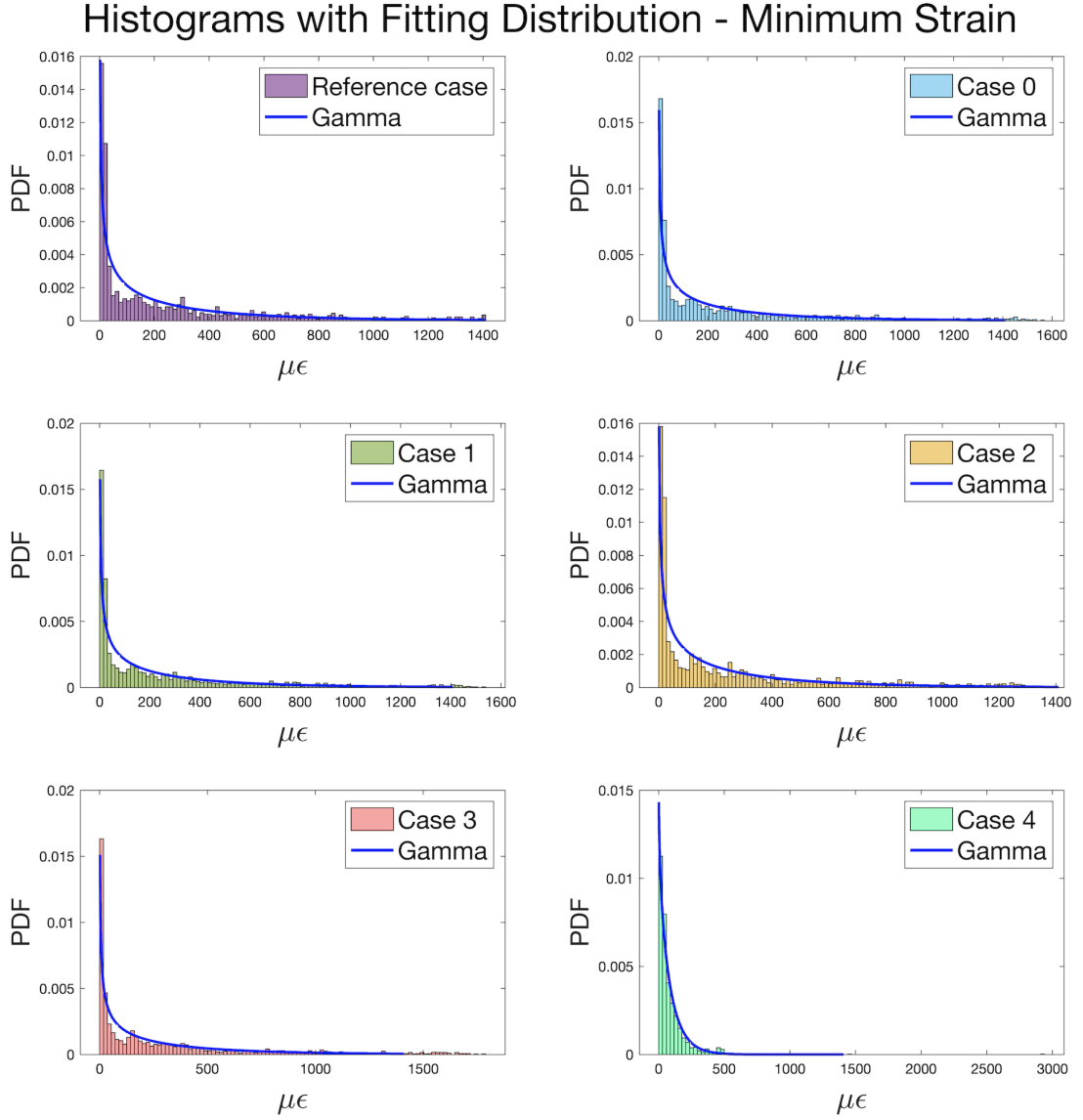


Figure 3.9: Histograms of deformation data overlaid with fitted gamma distribution curves. The y-axis represents the probability density function (PDF), while the x-axis shows $\mu\epsilon$ values. The fitted curves closely match the observed data distribution for minimum strains (ϵ_3) across all analyzed cases.

Table 3.3: p-values obtained from the Kolmogorov-Smirnov test comparing the maximum strains (ϵ_1) and the fitted distribution of the study cases with the reference case. p-values in the first column were derived directly from the distribution data, while p-values in the second column were derived from fitted distribution data.

Case	p-value (ϵ_1)	p-value (Fitted Distribution)
Case 0	0.965	1.000
Case 1	1.000	1.000
Case 2	0.750	1.000
Case 3	0.220	0.985
Case 4	0.003	0.0025

Table 3.4: p-values obtained from the Kolmogorov-Smirnov test comparing Case 0 with cases 1, 2, 3, and 4 for the maximum strains (ϵ_1) and the fitted distribution. p-values in the first column were derived directly from the distribution data, while p-values in the second column were derived from fitted distribution data.

Case	p-value (ϵ_1)	p-value (Fitted Distribution)
Case 1	1.000	1.000
Case 2	0.921	1.000
Case 3	0.082	0.985
Case 4	0.0032	0.0025

Table 3.5: p-values obtained from the Kolmogorov-Smirnov test comparing the minimum strains (ϵ_3) and the fitted distribution of the study cases with the reference case. p-values in the first column were derived directly from the distribution data, while p-values in the second column were derived from fitted distribution data.

Case	p-value (ϵ_3)	p-value (Fitted Distribution)
Case 0	0.988	1.000
Case 1	0.998	1.000
Case 2	0.720	1.000
Case 3	0.220	0.972
Case 4	0.0029	0.0017

Table 3.6: p-values obtained from the Kolmogorov-Smirnov test comparing Case 0 with cases 1, 2, 3, and 4 for the minimum strains (ϵ_3) and the fitted distribution. p-values in the first column were derived directly from the distribution data, while p-values in the second column were derived from fitted distribution data.

Case	p-value (ϵ_3)	p-value (Fitted Distribution)
Case 1	1.000	1.000
Case 2	0.572	1.000
Case 3	0.137	0.972
Case 4	0.0036	0.0017

Chapter 4

Conclusion

The prediction of femoral fractures using computational modeling raises important questions about the role of muscle forces in determining fracture risk. This study aimed to examine this issue in detail by exploring different approaches for transferring muscle forces from multibody models to finite element (FE) models. Using data obtained from simulations of static pose and muscle forces generated by a simplified musculoskeletal model, the influence of these forces on the femur was evaluated through an FE model. Five different boundary conditions were tested, and the results were compared to a reference model free of muscle forces.

Furthermore, conclusions were analyzed through detailed analyses of strain distributions using histograms and statistical testing with p-values. These analyses provided strong insights into the effects of muscle forces on femoral strain patterns. Particularly, the findings revealed that the presence or absence of muscle forces did not result in significant differences in strain distribution across the femoral surface. In conclusion, it is proposed that, for predictive purposes, the inclusion of muscle forces may be unnecessary, reducing model computational complexity and possibly improving simulation accuracy.

However, it is important to understand the current study's limitations, which include the use of a simplified model and the simulation of a static pose. Future developments could include increasing the number of muscles included in the analysis and simulating more dynamic activities to better understand the impact of muscle forces on femoral fracture risk.

Bibliography

- [1] «Compartment-specific effects of muscle strength on bone microarchitecture in women at high risk of osteoporosis». In: *Journal of Cachexia, Sarcopenia and Muscle* 13.5 (2022), pp. 2310–2321. DOI: 10.1002/jcsm.13044 (cit. on p. 1).
- [2] «Greater pQCT Calf Muscle Density Is Associated with Lower Fracture Risk, Independent of FRAX, Falls and BMD: A Meta-Analysis in the Osteoporotic Fractures in Men (MrOS) Study». In: *JBMR plus* 6.12 (2022). DOI: 10.1002/jbm4.10696 (cit. on p. 1).
- [3] Adam Stops, Ruth K. Wilcox, and Zhongmin Jin. «Computational modelling of the natural hip: a review of finite element and multibody simulations». In: *Computer Methods in Biomechanics and Biomedical Engineering* (2012) (cit. on p. 2).
- [4] «A multi-scale modelling framework combining musculoskeletal rigid-body simulations with adaptive finite element analyses, to evaluate the impact of femoral geometry on hip joint contact forces and femoral bone growth.» In: *PLOS ONE* 15.7 (2020), pp. 1–18. DOI: 10.1371/JOURNAL.PONE.0235966 (cit. on pp. 2, 4).
- [5] «Femoral neck strain prediction during level walking using a combined musculoskeletal and finite element model approach». In: *PLOS ONE* 16.2 (2021), pp. 1–19. DOI: 10.1371/JOURNAL.PONE.0245121 (cit. on pp. 2, 4–6, 17–20).
- [6] Giordano Valente, Gianluigi Crimi, Nicola Vanella, Enrico Schileo, and Fulvia Taddei. «nmsBuilder: Freeware to create subject-specific musculoskeletal models for OpenSim». In: *Computer Methods and Programs in Biomedicine* 152 (2017), pp. 85–92. ISSN: 0169-2607. DOI: <https://doi.org/10.1016/j.cmpb.2017.09.012>. URL: <https://www.sciencedirect.com/science/article/pii/S016926071730367X> (cit. on pp. 2, 3).
- [7] *Multibody modeling of the musculoskeletal system*. Elsevier eBooks, 2023, pp. 121–141. DOI: 10.1016/b978-0-12-823913-1.00008-7 (cit. on p. 3).

- [8] «Finite element models of the human shoulder complex: a review of their clinical implications and modelling techniques». In: *International Journal for Numerical Methods in Biomedical Engineering* 33.2 (2017). DOI: 10.1002/CNM.2777 (cit. on pp. 3, 4).
- [9] «OpenSim: Open-Source Software to Create and Analyze Dynamic Simulations of Movement». In: *IEEE Transactions on Biomedical Engineering* (2007). DOI: 10.1109/TBME.2007.901024 (cit. on pp. 3, 9, 12, 15, 16).
- [10] «The Multimod Application Framework». In: (2004). DOI: 10.1109/IV.2004.129 (cit. on p. 3).
- [11] «OpenSim: Simulating musculoskeletal dynamics and neuromuscular control to study human and animal movement.» In: *PLOS Computational Biology* (2018). DOI: 10.1371/JOURNAL.PCBI.1006223 (cit. on p. 3).
- [12] *Extended Finite Element Method: Theory and Applications*. 2015 (cit. on p. 4).
- [13] «Influence of muscle forces on femoral strain distribution». In: *Journal of Biomechanics* 31.9 (1998), pp. 841–846. DOI: 10.1016/S0021-9290(98)00080-3 (cit. on pp. 4, 8, 9, 16).
- [14] L. Modenese. «Webinar: Interfacing Musculoskeletal and Finite Element Models to Study Bone Structure and Adaptation». PhD thesis. Imperial College London, dic 2018. URL: https://www.youtube.com/watch?v=0e6vQV_ioCI (cit. on p. 5).
- [15] «Femoral Neck Strain during Maximal Contraction of Isolated Hip-Spanning Muscle Groups». In: *Computational and Mathematical Methods in Medicine* 2017 (2017), pp. 2873789–2873789. DOI: 10.1155/2017/2873789 (cit. on pp. 7, 17, 18).
- [16] «Mechanical Loading of the Femoral Neck in Human Locomotion». In: *Journal of Bone and Mineral Research* (2018). DOI: 10.1002/JBMR.3529 (cit. on p. 9).
- [17] Andrew D. Speirs, Markus O. Heller, Georg N. Duda, and William R. Taylor. «Physiologically based boundary conditions in finite element modelling». In: *Journal of Biomechanics* 40.10 (2007), pp. 2318–2323. ISSN: 0021-9290. DOI: <https://doi.org/10.1016/j.jbiomech.2006.10.038>. URL: <https://www.sciencedirect.com/science/article/pii/S0021929006004076> (cit. on pp. 10, 17–21).
- [18] *Gait2392 Opensim Documentation*. URL: <https://simtk-confluence.stanford.edu:8443/display/OpenSim/Gait+2392+and+2354+Models> (cit. on p. 12).

- [19] Katherine M Steele, Matthew S Demers, Michael H Schwartz, and Scott L Delp. «Compressive tibiofemoral force during crouch gait». In: *Gait & Posture* 35.4 (Apr. 2012). Epub 2011 Dec 27, pp. 556–560. DOI: 10.1016/j.gaitpost.2011.11.023 (cit. on p. 15).
- [20] R. J. van Arkel, L. Modenese, A. T. Phillips, and J. R. Jeffers. «Hip abduction can prevent posterior edge loading of hip replacements». In: *Journal of Orthopaedic Research* 31.8 (Aug. 2013). Epub 2013 Apr 10, pp. 1172–1179. DOI: 10.1002/jor.22364 (cit. on p. 15).
- [21] The MathWorks Inc. *Optimization Toolbox version: 9.4 (R2022b)*. Natick, Massachusetts, United States, 2022. URL: <https://www.mathworks.com> (cit. on p. 15).
- [22] «A multiscale model to predict current absolute risk of femoral fracture in a postmenopausal population». In: *Biomechanics and Modeling in Mechanobiology* (2019). DOI: 10.1007/S10237-018-1081-0 (cit. on pp. 17, 18).
- [23] Zainab Altai, Muhammad Qasim, Xinshan Li, and Marco Viceconti. «The effect of boundary and loading conditions on patient classification using finite element predicted risk of fracture». In: *Clinical Biomechanics* 68 (2019), pp. 137–143. ISSN: 0268-0033. DOI: <https://doi.org/10.1016/j.clinbiomech.2019.06.004>. URL: <https://www.sciencedirect.com/science/article/pii/S0268003319301925> (cit. on pp. 17, 18).
- [24] «Personalised 3D Assessment of Trochanteric Soft Tissues Improves HIP Fracture Classification Accuracy». In: *Annals of Biomedical Engineering* (2022). DOI: 10.1007/s10439-022-02924-1 (cit. on pp. 17, 18).